J. Meas. Sci. Instrum., 2026, 17(1): 72-87.
DOI: 10.62756/jmsi.1674-8042.2026006
http://jmsi.publish.founderss.cn
jmsi@nuc.edu.cn

Image processing method for defect images of ferromagnetic metal casings based on pulsed eddy current testing

DENG Yong[1,2*], SONG Dilin[1,2], SUN Hu[1,2]

1. School of Mechatronic Engineering, Southwest Petroleum University, Chengdu 610500, China;
2. Sichuan Science and Technology Resource Sharing Service Platform for Oil and Gas Equipment Technology, Chengdu 610500, China

***Corresponding author:** DENG Yong (201231010013@swpu.edu.cn)

Received: March 12, 2025 **Revised:** April 12, 2025 **Accepted:** May 11, 2025

Abstract: In oil and gas extraction, ferromagnetic metal casings serve as critical infrastructure to ensure the safety of hydrocarbon transport. However, under high-temperature and high-pressure conditions, casings buried deep underground are prone to deformation, twisting, and even rupture due to erosion and corrosion, potentially leading to significant economic losses and safety hazards. Therefore, regular inspection and maintenance of in-service well casings are essential. Pulsed eddy current testing (PECT) has been widely used for casing defect detection owing to its efficiency, non-contact nature, and rich information content. However, the presence of substantial noise during detection degrades the quality of defect detection images. To address this issue, we investigated image processing techniques for casing defect detection images and proposed an image processing algorithm (BIC) based on bidimensional empirical mode decomposition (BEMD), improved wavelet threshold denoising (IWTD), and contrast limited adaptive histogram equalization (CLAHE). The proposed method first applied BEMD-IWTD for noise suppression in defect detection images, followed by CLAHE for image enhancement. To validate the effectiveness of the method, defect detection experiments were conducted on casings with ring-shaped and local defects, and the acquired images were processed. After being processed with the BIC algorithm, ring-shaped defects of different depths could be effectively distinguished, especially the 1 mm and 2 mm deep defects that were previously affected by noise. In the local defect images, small-sized defects difficult to be identified due to noise interference were successfully recognized, and the defect contrast C_d was significantly improved. The results demonstrate that the proposed BIC algorithm effectively suppresses the noise in defect detection images, enhances the contrast between defects and the background, and improves defect recognition and detection accuracy, providing reliable image processing support for subsequent defect analysis.

Key words: ferromagnetic metal casing; nondestructive testing (NDT); pulsed eddy current testing (PECT); defect detection; image denoising; image enhancement

0 Introduction

Ferromagnetic metal casings are extensively used in the exploration and extraction of petroleum and natural gas, playing a crucial role in processes such as cementing, isolating formation water, and establishing oil and gas production pathways[1-3]. Due to factors such as formation pressure, downhole high temperature, and electrochemical corrosion, ferromagnetic metal casings are prone to deformation, twisting, wall thinning, and perforation of the casing body[4-6]. These issues may lead to the leakage of fluids (such as oil, natural gas, and drilling mud) from oil and gas wells, potentially causing wellbore instability and casing collapse. In severe cases, they may result in blowouts or fires, leading to significant economic losses and casualties. Therefore, it is imperative to conduct regular inspection, evaluation, and maintenance of in-service oil and gas well casings to ensure extraction safety, mitigate potential risks, and safeguard public safety and economic stability.

Nondestructive testing (NDT) techniques have been widely applied in casing defect detection owing to their ability to evaluate defects without causing damage to the inspected object[7]. Currently, common NDT methods include ultrasonic testing (UT), electromagnetic acoustic transducers (EMATs), pulsed eddy current testing (PECT), and remote-field eddy current testing (RFECT). Among these methods, UT offers high penetration depth and fast detection speed. However, its operation is relatively complex and requires the use of a couplant to ensure effective transmission of ultrasonic waves[8-10]. EMATs have the advantages of non-contact operation, no need for a couplant, and the ability to generate ultrasonic signals with different modes. However, interference from the tested object and the inherent performance limitations of EMATs can affect the quality of the ultrasonic signals[11]. RFECT offers the advantage of detecting defects on both the inner and outer walls of metal pipelines. However, the signals associated with these defects are weak and difficult to quantify due to the low-frequency excitation field penetrating the pipeline wall[12]. Additionally, in RFECT, the signal amplitude received by the pick-up coil is relatively small, and the eddy current signals related to defect size and shape are mixed with the induced magnetic field of the defects, leading to poor imaging quality, especially in complex environments[13].

Although existing NDT techniques offer various effective methods for detecting defects in oil and gas well casings, several challenges persist in inspecting deeply buried ferromagnetic metal casings. In such environments, severe signal attenuation occurs, while complex environmental noise significantly degrades signal quality. An effective defect assessment strategy involves leveraging the transient response characteristics of PECT. For example, Vasic et al. [14] and Xu et al. [15] found that the zero-crossing time and peak arrival time of the PECT time-domain response signal can be used to evaluate pipeline wall thickness. Ulapane et al. [16] proposed a PECT-based quantification method that determines the thickness of ferromagnetic pipelines by analyzing the attenuation rate of the PECT response signal. Compared to time-domain feature analysis, images generated from the transient response of PECT can effectively visualize defect information. Imaging provides spatial defect information, including size, shape, location, orientation, and distribution[17]. For example, Li et al.[18] utilized the amplitude of the PECT time-domain response to construct images of subsurface corrosion defects in aluminum alloy plates, improving imaging quality and detection sensitivity. Nafiah et al.[19] quantified the inclination and depth of cracks in aluminum plates using differential PECT response signals and effectively identified crack axes based on image feature extraction techniques, enabling feature extraction from linear scans. Yan et al.[20] employed the maximum amplitude of the PECT differential response signal for corrosion defect imaging of aluminum alloy plates and proposed an improved Canny algorithm to process corrosion images, enhancing corrosion morphology recognition. Li et al.[21] used the peak value of the PECT time-domain response signal to image external corrosion defects in non-ferromagnetic aluminum alloy pipelines, improving the sensitivity of external corrosion assessment and the accuracy of corrosion imaging. Xie et al. [22] employed PECT to detect surface cylindrical wall-thinning defects on the outer wall of the main pipe in a double-layered pipeline structure and constructed 2D scan pickup signals to detect wall thickness reduction.

Although the aforementioned methods are effective, the complex on-site environment in actual pipeline inspections introduces significant noise, which degrades the imaging quality of defect detection and complicates subsequent defect analysis. To address this issue, various image processing algorithms have been employed to reconstruct defect detection images with enriched defect information. Zhu et al. [23] proposed a novel feature extraction method based on image entropy and fusion, which preserves more defect information while effectively suppressing background noise. Yan et al.[24] developed an improved image processing technique based on the theta map for reconstructing corrosion profiles within corroded regions. Li et al.[25] introduced a weighted estimation algorithm, and experimental results show that the proposed method significantly enhances defect edge clarity. Ren et al. [26] proposed an image processing algorithm combining sparse Bayesian learning (SBL) with baseline estimation and denoising with sparsity (BEADS) to reconstruct corrosion images and extract information about corrosion depth profiles. Zhu et al. [27] designed a differential PECT probe to reduce lift-off noise in PECT signals and introduced a mask-based image segmentation and refinement method, which effectively eliminates blurring effects in defect detection images. Balakrishnan et al.[28] utilized an eddy current image fusion method based on discrete wavelet transform. Their fusion results demonstrate that appropriate wavelet and fusion rule selection reduces blurring and enhances the reliability of defect detection in both visual and qualitative evaluations.

However, current studies have paid little attention to the impact of external noise in PECT, particularly the effective countermeasures against noise. Moreover, in practical applications, defect images often suffer from blurriness and low contrast, which hinders feature identification. To address these challenges in detecting defects in deeply buried ferromagnetic casings, a casing defect detection prototype was designed based on the amplitude of the transient response signal in the pick-up coil. The prototype was placed inside the casing for defect detection, utilizing pulsed eddy current transient response features to generate defect detection images. To denoise and enhance image clarity, this study introduced a casing defect detection image processing algorithm based on BEMD-IWTD-CLAHE (BIC). First, the defect detection image was decomposed using bidimensional empirical mode decomposition (BEMD) into intrinsic mode function (IMF) sub-images of different characteristic scales. Then, improved wavelet threshold denoising (IWTD) was applied to the high-frequency IMF components. The denoised IMF sub-images were then recombined with the residual sub-images to reconstruct the denoised defect image. Finally, contrast limited adaptive histogram equalization (CLAHE) was employed to enhance the contrast and visual quality of the image. The defect detection image processing results indicate that, compared with various image processing methods, the proposed method effectively denoises the image and enhances the contrast between defects and the background.

1 Principle of pulsed eddy current casing defect detection and algorithm model

1.1 Principle of pulsed eddy current casing defect detection

The defect detection method based on the transient response of PECT applies a pulsed current to the driver coil, generating a changing electromagnetic field. This field induces eddy currents inside the metallic casing. The induced eddy currents form closed loops, which in turn generate a secondary magnetic field. The strength of this magnetic field depends on the casing's electromagnetic properties and physical dimensions. For the same ferromagnetic casing, its electromagnetic properties remain unchanged. The main factor affecting the magnetic field is casing defects. These defects disrupt the eddy currents, changing the magnetic field distribution. By analyzing these changes, casing defects can be detected. An array of pick-up coils is used to detect local defects. The detection schematic is shown in Fig.1.

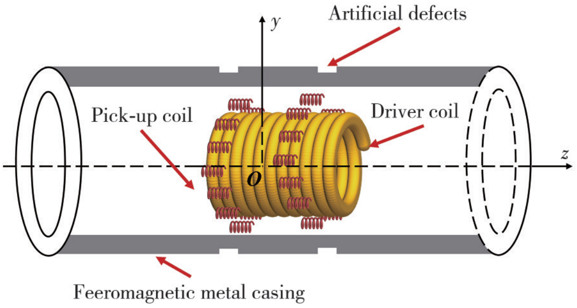

(a) 3D schematic diagram

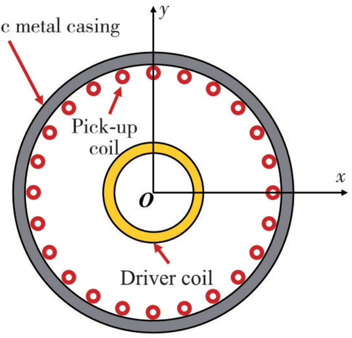

(b) 2D schematic diagram

Fig. 1 Detection of local casing defects using an array of pick-up coils

Existing studies have shown that induced eddy currents in the metal casing wall tend to flow toward the areas with lower electrical resistance over time. If a defect is present in the near-field region of the casing wall, the reduced wall thickness in that area will result in higher resistance. After a certain period, the eddy current density around the defect will be higher than that at the defect itself. The lower eddy current density at the defect leads to a decrease in the amplitude of the eddy current response signal in the pick-up coil. Consequently, the response signal amplitude in the defect regions will be lower than that in the areas with normal wall thickness. Therefore, the amplitude of the pulsed eddy current transient response can be effectively used to detect casing defects.

1.2 BIC algorithm model

1.2.1 BEMD theory

BEMD is an extension of one-dimensional empirical mode decomposition (EMD). Unlike traditional wavelet decomposition, BEMD does not require a predefined basis function. Instead, it adaptively extracts image details at different feature scales through an iterative sifting process. The BEMD of a 2D image $f(x,y)$ follows these steps[29].

Step 1 Initialization. Setting $fr_{n,m-1}(x,y)=f(x,y)$ as the input image, and initializing n to 1 and m to 1.

Step 2 Identification of local maxima and minima of $fr_{n,m-1}(x,y)$. Constructing the upper envelope $e^{\max}_{n,m-1}(x,y)$ and the lower envelope $e^{\min}_{n,m-1}(x,y)$ based on these extrema and computing their mean surface as by

$$Z_{n,m}(x,y)=\frac{e^{\max}_{n,m-1}(x,y)+e^{\min}_{n,m-1}(x,y)}{2}. \tag{1}$$

Step 3 By subtracting the mean envelope surface from the input image, we can obtain

$$P_{n,m-1}(x,y)=fr_{n,m-1}(x,y)-Z_{n,m-1}(x,y). \tag{2}$$

Step 4 Determining whether $P_{n,m-1}(x,y)$ satisfies IMF constraint condition $\sigma_{\mathrm{SD}}<\varepsilon$, where σ_{SD} refers to standard deviation. If the condition is not met, setting $m=m+1$to update

$$fr_{n,m-1}(x,y)=P_{n,m-2}(x,y),\tag{3}$$

and returning to step 2, followed by repeating this process until the constraint condition is satisfied after k iterations. If the condition is met, the nth intrinsic mode function $f_{n(x,y)}^{\mathrm{IMF}}$ is given by $P_{n,m-1}(x,y)$, where the standard deviation is obtained by

$$\sigma_{\mathrm{SD}}=\sum_{x=0}^{i}\sum_{y=0}^{j}\frac{\left|fr_{n,m-1}(x,y)-P_{n,m-1}(x,y)\right|^{2}}{\left[fr_{n,m-1}(x,y)\right]^{2}}.\tag{4}$$

Step 5 Obtaining the residual component $P_{n,m-1}(x,y)$, and setting $n=n+1$ and $fr_{n,0}(x,y)=fr_{n-1,0}(x,y)-f_{n-1}^{\mathrm{IMF}}(x,y)$. If the number of extrema in the residual component is greater than 2, $fr_{n,0}(x,y)$ is treated as a new image and the algorithm returns to step 2 to continue the decomposition. Otherwise, the decomposition terminates, and the final residual component is $fr_k(x,y)$. Thus, the reconstructed image can be expressed as

$$f(x,y)=\sum_{i=1}^{k}f_i^{\mathrm{IMF}}(x,y)+fr_k(x,y).\tag{5}$$

1.2.2 IWTD

The wavelet threshold denoising was first proposed by Donoho et al. in 1992. It is primarily based on wavelet transform and the principle of sparse representation. Wavelet transform enables the decomposition of a signal into sub-bands with different frequency components. The high-frequency coefficients obtained from the decomposition are then processed using a thresholding function. Finally, the signal is reconstructed by combining the scale coefficients and the threshold-processed high-frequency coefficients, yielding a denoised signal. The commonly used thresholding functions in wavelet threshold denoising are the hard threshold function and the soft threshold function, which are expressed as follows.

The hard threshold function is given by

$$h_{j,k}=\begin{cases}w_{j,k}, & |w_{j,k}|>\lambda_j,\\ 0, & |w_{j,k}|\leqslant\lambda_j,\end{cases}\tag{6}$$

where $q_{j,k}$ represents the wavelet coefficients processed by the threshold function.

The soft threshold function is given by

$$s_{j,k}=\begin{cases}\operatorname{sgn}(w_{j,k})(|w_{j,k}|-\lambda_j), & |w_{j,k}|>\lambda_j,\\ 0, & |w_{j,k}|\leqslant\lambda_j,\end{cases}\tag{7}$$

where sgn(•) is a sign function.

To overcome the limitations of hard and soft threshold functions, we propose an improved threshold function. This function can adjust the degree of softness and hardness according to the actual signal. It also features a concise expression and symmetric structure. The expression is given by

$$q_{j,k}=\begin{cases}w_{j,k}-\beta\operatorname{sgn}(w_{j,k})\dfrac{\lambda^{\alpha}}{|w_{j,k}|^{\alpha-1}}, & |w_{j,k}|>\lambda_j,\\[2ex] \beta\operatorname{sgn}(w_{j,k})\dfrac{|w_{j,k}|^{\alpha+1}}{\lambda^{\alpha}}, & |w_{j,k}|\leqslant\lambda_j,\end{cases}\tag{8}$$

where λ_j is calculated by

$$\lambda_j=\frac{\sigma\sqrt{2\lg N}}{\lg(j+1)},\tag{9}$$

where N represents the number of wavelet coefficients at the corresponding scale, and σ denotes the noise intensity, which is estimated by

$$\sigma=\frac{\sigma_{\mathrm{MAD},j,k}}{0.6745},\tag{10}$$

where $\sigma_{\mathrm{MAD},i,j}$ represents the median of the absolute deviations of the wavelet coefficients in the kth sub-band at scale j.

In the improved threshold function, α is a variable parameter. To ensure the continuity of the threshold function, calculations show that β must be equal to 0.5. The parameter α controls the nonlinearity of the threshold function and can be any real number greater than 1. When $\alpha=1$, the threshold function is almost identical to the soft threshold function. When α is too large, the function curve approaches that of the hard threshold function. By adjusting the values of α, the new threshold function can achieve a smooth transition from noise coefficients to signal coefficients during wavelet threshold denoising. To visually illustrate the impact of parameter variations on the threshold function, we set $\beta=0.5$ and $\alpha\in[2,15]$, and plots the threshold function with a gradient of 2, as shown in Fig. 2. When the threshold and β remain constant, the improved threshold function can be represented as both soft and hard threshold functions depending on the value of α. Regardless of the chosen α, the function maintains continuity. When α is relatively large, the function is more suitable for processing noisy signals with a high signal-to-noise ratio (SNR). Conversely, a smaller α results in more wavelet coefficients in the critical region, allowing better retention of fine signal details while suppressing noise coefficients. This helps preserve the original local singularities of the signal. Finally, by iteratively adjusting the parameter α, the optimal denoising performance can be achieved.

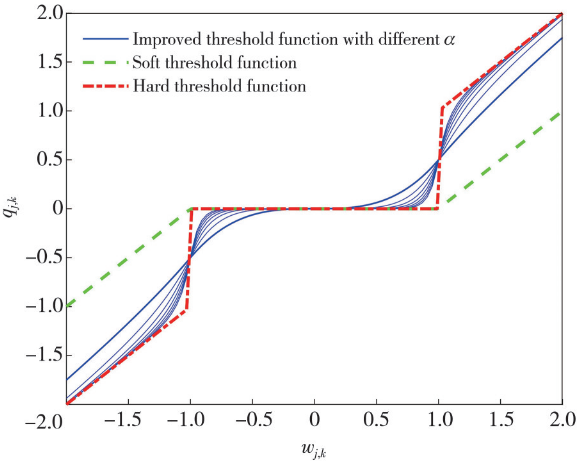

Fig. 2 Comparison of soft, hard, and improved threshold functions

1.2.3 Contrast-limited adaptive histogram equalization

In image denoising, although denoising algorithms can effectively remove noise, they often introduce image blurring, especially in defect detection images with low SNR. CLAHE enhances the visualization of local details by increasing the contrast in small regions. In this study, CLAHE is applied to defect detection images generated from the amplitude characteristics of pulsed eddy current transient responses. This enhances the visibility of defects, making them easier to identify and improving the overall defect detection visualization. CLAHE first divides the image into several sub-regions, applies histogram equalization to each sub-region, and then merges them back into their original positions in the image. By adapting to local image features, CLAHE effectively enhances visual quality, particularly in cases where the contrast between the background and defects is not prominent.

1.2.4 BIC algorithm process

During the PECT process, the original signals are often affected by practical testing conditions and equipment limitations, such as mechanical vibrations of the instrument, ambient electromagnetic interference, and circuit system noise. These interferences introduce substantial noise into the acquired signals, which in turn results in defect detection images contaminated with a large amount of noise. In these images, the energy of defect-related signals is primarily concentrated in the low-frequency domain, while noise is predominantly distributed in the high-frequency domain. PECT response signal is typically nonlinear and nonstationary in nature, posing considerable challenges for subsequent defect identification. Given the diversity and complexity of such interferences, a single image processing technique often fails to simultaneously suppress noise and preserve defect-related information.

Therefore, BIC algorithm with clearly defined functional roles and synergistic effects is proposed in this study. Specifically, BEMD is first employed to decompose the defect images under detection. BEMD does not rely on assumptions of linearity or stationarity and can adaptively extract IMF components at multiple spatial scales, making it well-suited for handling the complex and variable signal characteristics of defect images under detection. In the decomposition results, high-frequency IMFs primarily contain interference introduced by external noise, while low-frequency components tend to preserve more useful structural and defect-related information. However, since PECT signals are inherently weak, important edge and texture features related to defects may also be distributed in certain high-frequency components. Simply discarding these components would inevitably lead to the loss of valuable defect information. To address this issue, IWTD is introduced to perform fine-grained denoising on the high-frequency IMF components. By optimizing the threshold function, IWTD effectively suppresses noise while preserving critical image features such as edges and textures, thereby mitigating the over-smoothing problem commonly observed in traditional wavelet denoising methods.

After denoising, considering that defect images under detection often suffer from low contrast and difficulty in separating defect signals from the background, CLAHE is further employed to enhance the denoised image. This algorithm adaptively adjusts the histogram based on the local grayscale distribution, significantly improving local contrast and enhancing the distinction between the defect areas and the background, thereby improving defect visibility.

The proposed algorithm is a targeted image processing framework tailored to the nonstationary, weak, and low-contrast characteristics of defect detection images. By constructing images with the feature values acquired by the testing instrument as pixel intensities, the proposed algorithm achieves effective noise suppression and contrast enhancement, preserving more defect details while improving overall image quality. The algorithm flowchart is shown in Fig.3.

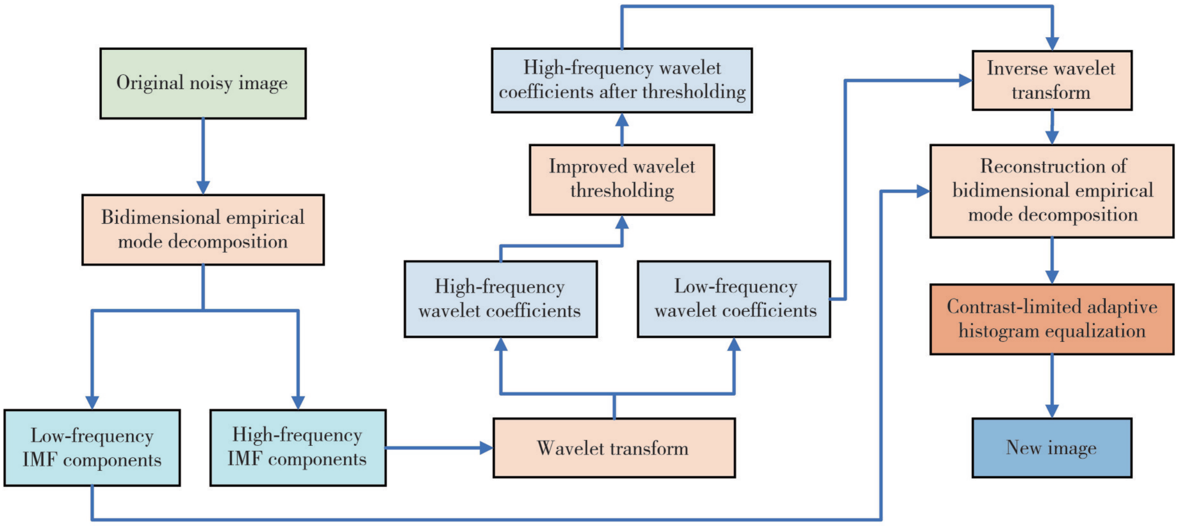

Fig. 3 Flowchart of BIC algorithm

2 Simulation

To verify the performance of the proposed image processing algorithm, we first investigated the effect of different wavelet base functions on the denoising performance of IWTD method based on BEMD. In the simulation, three types of wavelet bases—sym, db, and coif—were used to denoise a pulsed eddy current infrared image with added Gaussian white noise (mean is 0, variance is 0.01). The pulsed eddy current infrared image used in the simulation is shown in Fig. 6(a). The denoising performance of the algorithm is evaluated using two metrics: mean squared error (MSE) and peak signal-to-noise ratio (PSNR). The MSE is given by

$$e_{\mathrm{MSE}}=\frac{\sum_{x=1}^{m}\sum_{y=1}^{m}\left(f'(x,y)-f_{\mathrm{d}}(x,y)\right)^{2}}{m\times n}, \tag{11}$$

where $m\times n$ represents the image size, $f'(x,y)$ is the noise-free image, and $f_{\mathrm{d}}(x,y)$ is the denoised image.

The PSNR is given by

$$R_{\mathrm{PSN}}=10\lg\frac{R^{2}}{e_{\mathrm{MSE}}}, \tag{12}$$

where R represents the grayscale level of the image, with a value of 255.

Setting the wavelet decomposition level to three, the denoising results using different wavelet bases were obtained through simulation. As shown in Tables 1–3, the denoising performance of the db and sym wavelet bases is superior to that of the coif wavelet base. The best denoising results are achieved using the db8, sym9, and coif4 wavelet bases. This paper performed denoising at different decomposition levels using db8, sym9, and coif4 wavelet bases to verify the optimal decomposition level. As shown in Figs. 4 and 5, the optimal decomposition level is a three-layer wavelet decomposition, where the PSNR is the highest and the MSE is the lowest. Among different decomposition levels, sym9 exhibits better denoising performance than the other wavelet bases. Therefore, this study adopts the sym9 wavelet base for denoising.

Table 1 Denoising results of db wavelet base

db wavelet base	PSNR	MSE
1	33.692 0	27.789 2
2	34.275 7	24.294 8
3	34.553 1	22.791 2
4	34.566 6	22.720 6
5	34.605 8	22.516 7
6	34.686 8	22.100 3
7	34.606 3	22.513 9
8	34.740 7	21.827 9
9	34.604 3	22.524 2
10	34.726 1	21.901 3

Table 2 Denoising results of sym wavelet base

sym wavelet base	PSNR	MSE
1	33.692 0	27.789 2
2	34.275 7	24.294 8
3	34.553 1	22.791 2
4	34.639 9	22.340 2
5	34.573 4	22.684 9
6	34.751 0	21.776 0
7	34.620 6	22.440 1
8	34.718 5	21.939 8
9	34.767 1	21.695 3
10	34.647 2	22.302 6

Table 3 Denoising results of coif wavelet base

coif wavelet base	PSNR	MSE
1	34.325 1	24.019 9
2	34.644 0	22.319 3
3	34.634 7	22.367 3
4	34.735 2	21.855 5
5	34.695 2	22.057 8

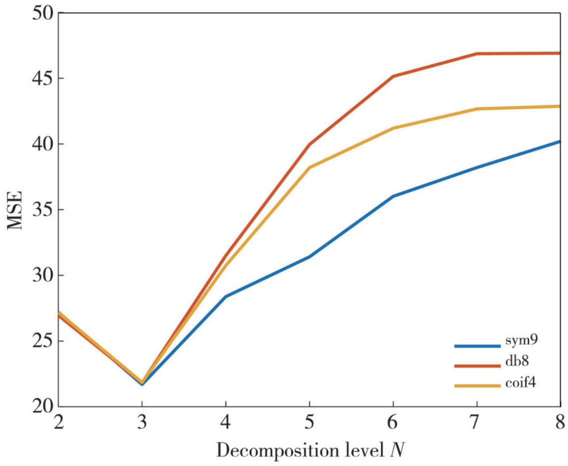

Fig. 4 Comparison of MSE at different decomposition levels

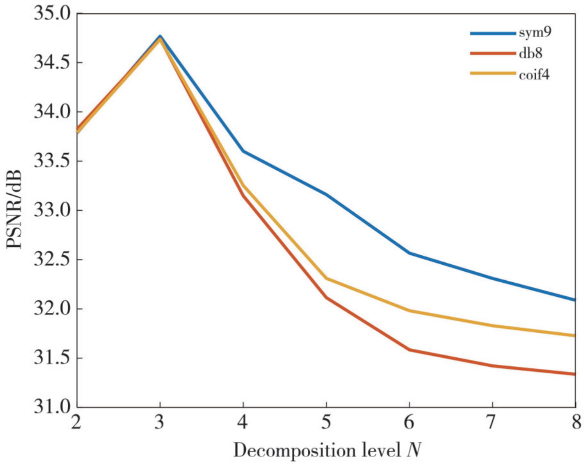

Fig. 5 Comparison of PSNR at different decomposition levels

The wavelet soft threshold denoising (WSTD), BEMD, IWTD, and the proposed BEMD-IWTD method were applied to the noisy pulsed eddy current infrared image shown in Fig. 6(b) to verify the effectiveness of the proposed algorithm.

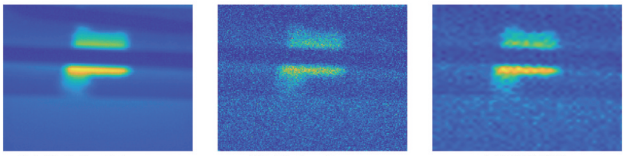

(a) Original image (b) Noisy image (c) WSTD

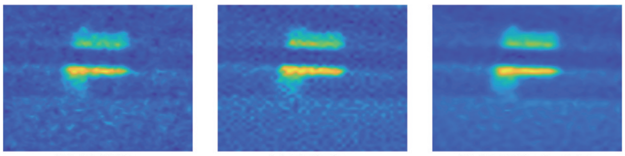

(d) BEMD (e) IWTD (f) BEMD-IWTD

Fig. 6 Comparison of image denoising effects using different algorithms for pulsed eddy current thermography

The proposed BEMD-IWTD method achieves the best image denoising results, effectively removing noise while preserving the detailed features of the defect regions. In contrast, direct BEMD denoising suppresses noise to some extent but results in significant detail loss, making the image blurry. Although WSTD can denoise to a certain extent, it causes image distortion, which compromises the integrity of defect information. In comparison, IWTD preserves more defect details and minimizes the loss of useful information. As shown in Table 4, compared with WSTD, BEMD, and IWTD, the BEMD-IWTD algorithm achieves the highest PSNR and the lowest MSE, significantly enhancing the image denoising performance and demonstrating its superiority.

Table 4 Comparison of denoising metrics for pulsed eddy current thermal imaging

Algorithm	PSNR	MSE
Noisy image	20.939 0	523.819 7
WSTD	31.909 0	41.897 0
BEMD	25.584 9	179.715 5
IWTD	32.584 5	38.658 1
BEMD-IWTD	34.767 1	21.695 3

To illustrate the advantages of the proposed BIC image processing algorithm, the denoised image obtained using BEMD-IWTD to achieve the best denoising performance was used as the input. Then, the CLAHE, histogram equalization (HE), and gramma transformation (GT) algorithms were employed to enhance the denoised image, and their effects were compared and analyzed. Fig. 7 presents the results obtained using different enhancement algorithms.

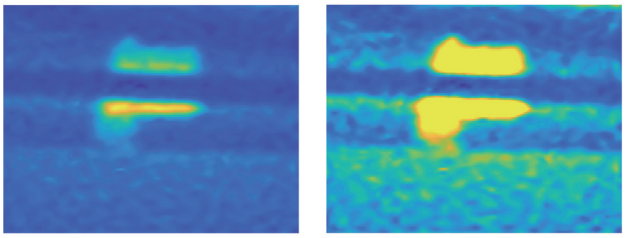

(a) BEMD-IWTD (b) BEMD-IWTD-GT

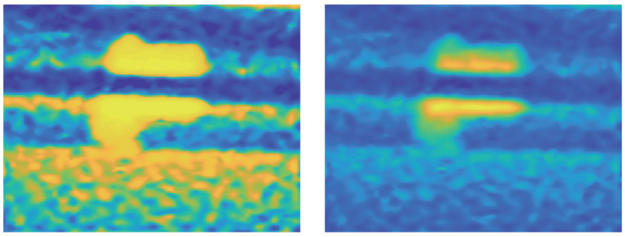

(c) BEMD-IWTD-HE (d) Proposed BIC algorithm

Fig. 7 Comparison of different enhancement algorithms after denoising in pulsed eddy current thermography

A subjective evaluation first indicates that the proposed BIC algorithm effectively reduces noise in defect images while significantly enhancing the contrast of defect regions, making defect information clearer. For the HE algorithm, although it can effectively enhance the contrast of defect regions, the background noise is also enhanced, affecting the clarity and recognizability of defects. In contrast, the GT algorithm can enhance the contrast of defects but tends to over-enhance defect regions, potentially introducing artifacts.

To quantitatively evaluate the improved defect detection images, the contrast between the target object and the background is a commonly used metric in natural image processing Refs. [30-32]. The average contrast between the defect and the background is used as the evaluation metric[33], which is defined as

$$C_{\mathrm{d}} = \frac{\sum_{i=1}^{m} S_{\mathrm{dr}}^{(i)}}{m} - \frac{\sum_{j=1}^{n} S_{\mathrm{non}}^{(j)}}{n}, \tag{13}$$

where m represents the number of pixels in the labelled defect region, $S_{\mathrm{dr}}^{(i)}$ represents the gray level of the ith pixel, $\sum_{i=1}^{m} S_{\mathrm{dr}}^{(i)}/m$ represents the average grey level in the defect region, n represents the number of pixels in the non-defect region, $S_{\mathrm{non}}^{(j)}$ represents the grey level of the jth pixel, and $\sum_{j=1}^{n} S_{\mathrm{non}}^{(j)}/n$ represents the average gray level in the non-defect region. The other metric used to evaluate image enhancement in this study is the structural similarity index (SSIM), which is defined as

$$SSIM(x,y) = \frac{(2\mu_x\mu_y + C_1)(2\sigma_{xy} + C_2)}{(\mu_x^2 + \mu_y^2 + C_1)(\sigma_x^2 + \sigma_y^2 + C_2)}, \tag{14}$$

where μ_x and μ_y represent the mean luminance of images x and y, respectively; σ_x^2 and σ_y^2 denote the variances of images x and y, respectively, while $2\sigma_{xy}$ represents the covariance between the two images; C_1 and C_2 are two small constants introduced to avoid division by zero. Generally, the closer the SSIM value is to 1, the more similar the two images are.

As shown in Table 5, although the BEMD-IWTD-HE and BEMD-IWTD-GT algorithms can enhance the defect contrast in pulsed eddy current defect detection images, they also cause severe image distortion and excessively amplify background noise, which significantly affects the accuracy of subsequent feature extraction and defect identification.

Table 5 Comparison of metrics for different enhancement algorithms after denoising in pulsed eddy current thermography

Algorithm	SSIM	C_{d}
BEMD-IWTD	1.000 0	0.273 1
BEMD-IWTD-GT	0.622 1	0.342 7
BEMD-IWTD-HE	0.401 5	0.389 3
BIC	0.952 9	0.352 1

In contrast, BIC algorithm effectively reduces noise in pulsed eddy current thermographic images while preserving the structural information of the original image and enhancing the contrast in defect regions. The defect information becomes clearer, facilitating subsequent automatic recognition and analysis.

3 Experiment

3.1 Experimental setup

A corresponding experimental system was built to evaluate the effectiveness of the proposed image processing method in practical defect detection. The experimental system is shown in Fig. 8(a), which includes a locally defective casing, a ring-shaped defective casing, a detection prototype, and a pulley system with a lead screw slide table to move the detection prototype inside the metal casing.

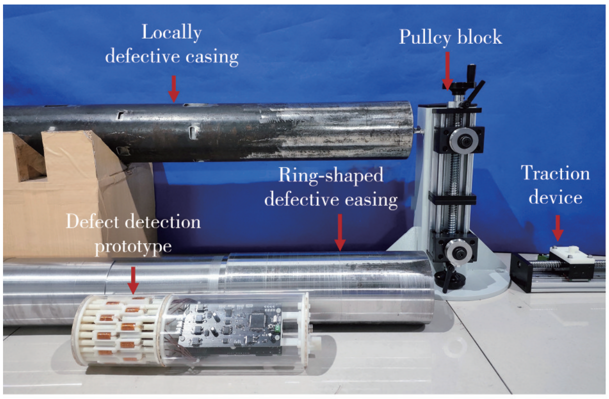

(a) Experimental system

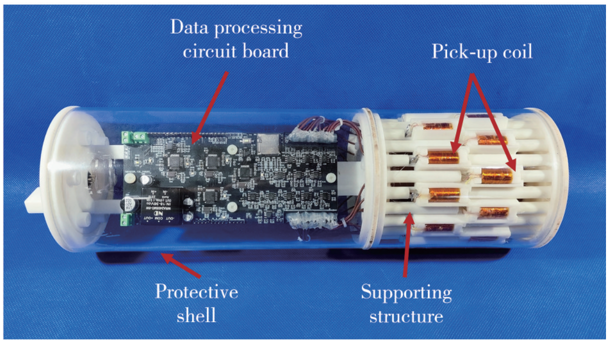

(b) Casing defect detection prototype

Fig. 8 Pulsed eddy current array coil testing on ferromagnetic metal casings

The prototype of the detection instrument is shown in Fig.8(b). The system operates with a DC power supply providing a voltage of 15 V. The detection prototype consists of an array of pick-up coils, a driver coil, an excitation circuit module, and a data processing circuit module. The framework of the detection prototype is manufactured using 3D printing with ABS resin. A specially designed mechanical structure supports the driver coil and pick-up coils, minimizing eccentricity and ensuring close contact with the inner wall of the casing to enhance signal acquisition stability and detection accuracy. During detection, the excitation circuit generates a pulsed excitation signal with a rise/fall time of approximately 3 ns. The received signal is amplified by the data processing circuit and acquired via ADC for subsequent defect detection image generation. A lead screw motor is used as the power source, pulling the detection prototype through the inner wall of the metal casing at a constant speed via the pulley system. The acquired detection data undergo filtering, storage, transmission, and processing to ultimately generate defect detection images.

In Fig. 9, the upper pipeline represents the metallic casing with local defects, and the lower pipeline represents the metallic casing with ring-shaped defects. For the ring-shaped defects, the defect depths are 1 mm, 2 mm, 3 mm and 5 mm, with each ring-shaped defect having a length of 20 cm.

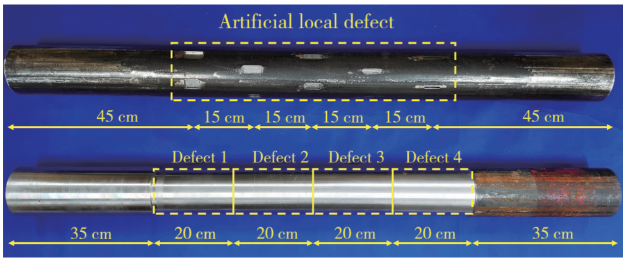

Fig. 9 Ferromagnetic pipes with defects

In the metallic casing with local defects, a total of 25 artificial defects are designed, distributed in 5 columns, with 5 defects per column. From left to right, the lengths of the local defects are 50 mm, 40 mm, 30 mm, 20 mm, and 10 mm, and the widths are 25 mm, 20 mm, 15 mm, 10mm, and 5 mm, respectively; All local defects have a depth of 6 mm. The position of the local defects on the outer surface of the casing is shown in Fig.10.

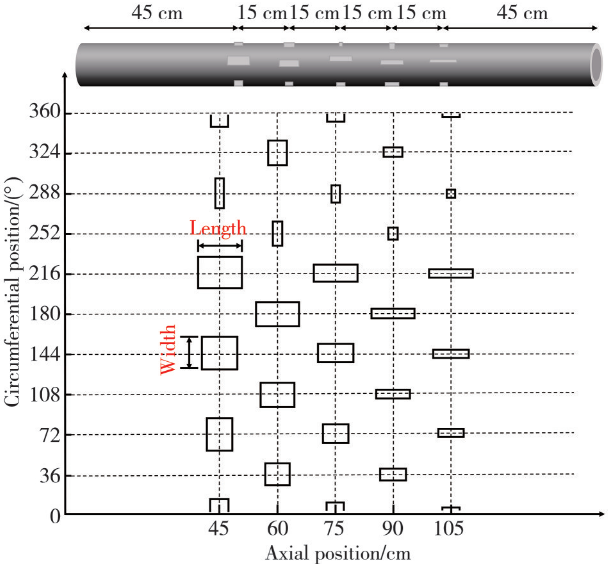

Fig. 10 Schematic diagram of distribution of local defects in casing

For convenience, the local defects in each column are labeled as Defect 1, Defect 2, Defect 3, Defect 4, and Defect 5, according to the defect volume from the largest to the smallest.

3.2 Results and discussion

3.2.1 Casing defect detection imaging

In the experiment, the tested casing was kept in a horizontal position, and the sample was dragged along the inner wall of the casing at a constant low speed using a lead screw traction device. The pulse excitation signal frequency was set to 10 Hz, corresponding to a movement of approximately 4.2 mm per detection cycle. The experiment was conducted to detect both annular and localized defects. This paper uses M, defined as the average value of the logarithmic curve of the transient response signal within 0.5 ms after 10 ms as the defect detection feature to generate defect reconstruction images.

For the ring-shaped defect detection, the detection prototype scanned the casing with pre-set ring-shaped defects and reconstructed the defect detection image, as shown in Fig.11(a). The different depths of annular defects exhibit distinct separations in the detection image, and the signal response of each annular defect significantly differs from that of the normal casing wall, providing a reference for subsequent localized defect detection.

For the localized defect detection, the array signals collected by the pick-up coils were analyzed to reconstruct localized defect images, as shown in Fig. 11(b). The observations reveal that some smaller defects are not effectively identified. For example, Defect 5, with a width of 5 mm and a length of 10 mm (a volume of 0.3 cm^3), and another defect with a width of 10 mm and a length of 10 mm (a volume of 0.6 cm^3), are not detected. By analyzing the defect detection images, it can be observed that a significant amount of background noise is present. This noise not only interferes with the visualization of defects but also obscures their true characteristics, thereby affecting subsequent defect identification and evaluation. Moreover, the presence of noise reduces the SNR, makes defect feature extraction more challenging, and impacts the automation and quantitative assessment of defect analysis. To improve the quality and reliability of defect detection images, we introduce the BIC image processing method to effectively suppress background noise, enhance defect features, and provide a clearer image data foundation for subsequent defect feature extraction and classification.

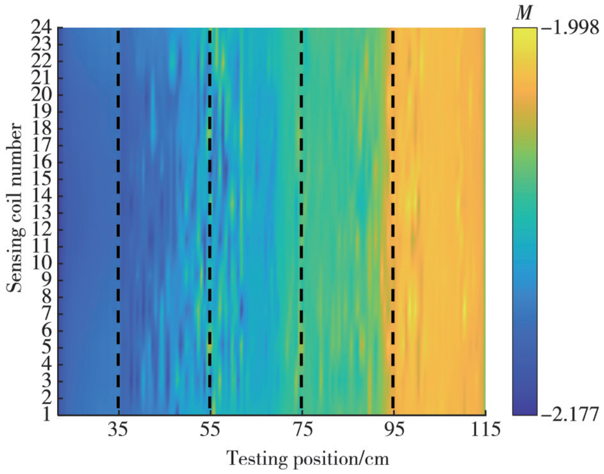

(a) Ring-shaped defects

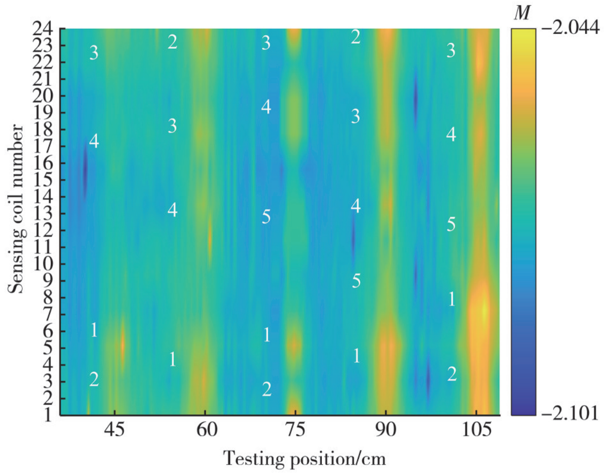

(b) Local defects

Fig. 11 Casing defect detection images

3.2.2 Experimental analysis of BIC algorithm

From the ring-shaped defect detection image, it can be observed that there is significant noise interference in the detection image, especially for ring-shaped defects at depths of 1 mm and 2 mm. The noise impact causes the spacing between defects to become unclear. For the local defect detection image, the defect signals are heavily disturbed by noise, particularly for smaller defects whose signals are almost completely overwhelmed by noise, such as Defect 3 and Defect 4 at 45 cm, and Defect 4 and Defect 5 at 75 cm. The presence of noise severely affects the visualization of defects, thereby reducing the accuracy of subsequent defect identification. To effectively suppress noise and enhance defect features, we introduce the BIC image processing method for the first time to optimize defect detection images generated from pulse eddy current defect features.

The defect detection images processed by the algorithm proposed in this study are shown in Fig. 12. After processing, the noise in the ring-shaped defect detection image is significantly suppressed, especially for the 1 mm and 2 mm deep circumferential defects, where the issue of unclear spacing due to noise interference is effectively improved. For the local defect detection image, the defect areas are more clearly identified, especially the small defects that are difficult to distinguish due to noise interference (e.g., Defect 3 and Defect 4 at 45 cm), which are now more clearly visible in the processed image. Additionally, the local defects at 75 cm show further improvement in contrast after enhancement, with the defect areas forming a more distinct visual difference from the background. The results above demonstrate that the BIC method proposed in this study not only effectively suppresses noise interference but also enhances the contrast between the defect areas and the background, thereby improving the visualization and recognizability of defects. This improvement is of great significance for subsequent manual defect assessment and automatic feature extraction.

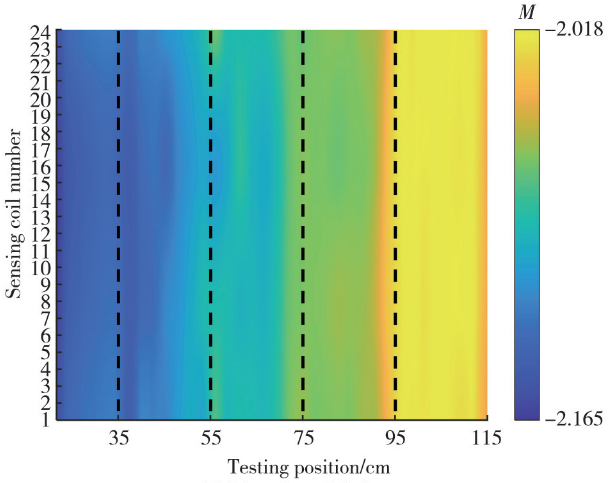

(a) Ring-shaped defects

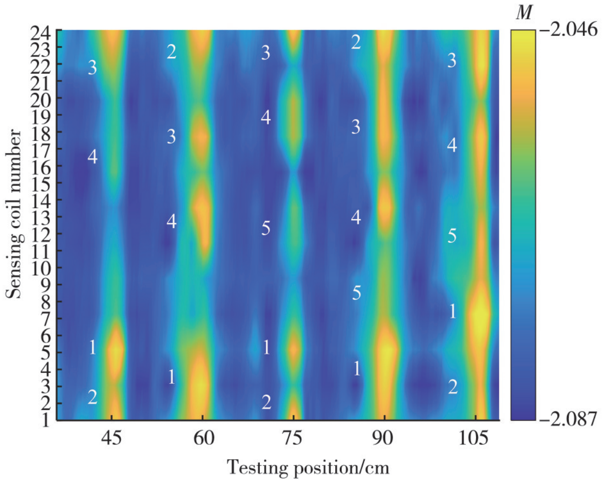

(b) Local defects

Fig. 12 Defect detection images processed using BIC algorithm

3.2.3 Performance comparison

This study applied WSTD, IWTD, BEMD, and BEMD-IWTD to defect detection images for comparative analysis to evaluate the effectiveness and performance of the proposed BIC image processing algorithm.

The denoised results for ring-shaped and local defects are shown in Figs.13 and 14, respectively.

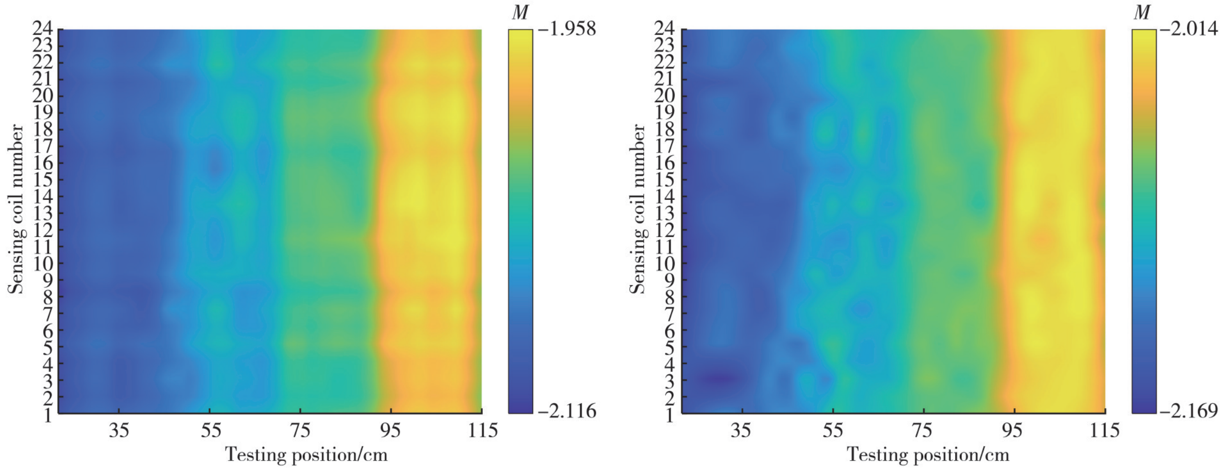

(a) WSTD (b) BEMD

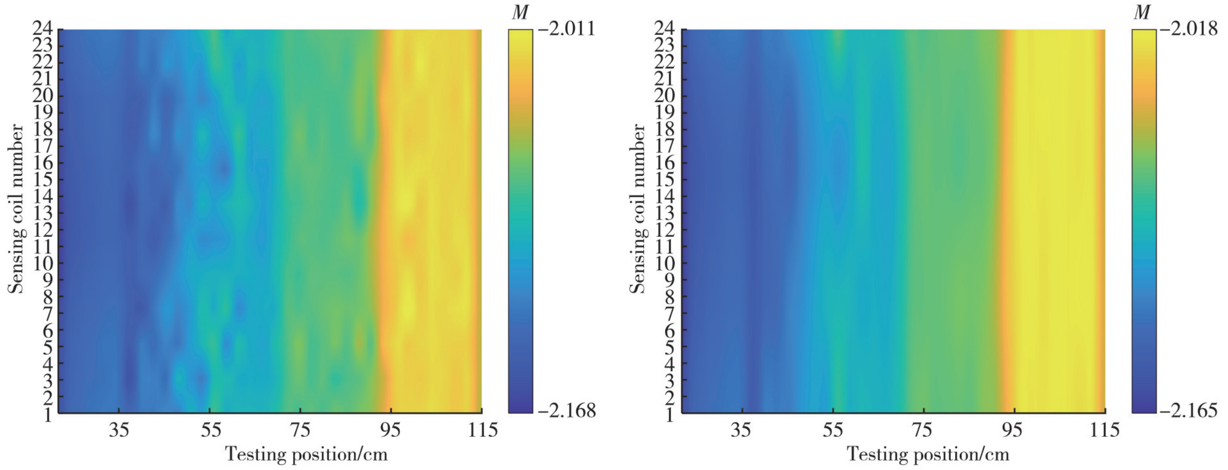

(c) IWTD (d) BEMD-IWTD

Fig. 13 Comparison of ring-shaped defect detection images using different denoising algorithms

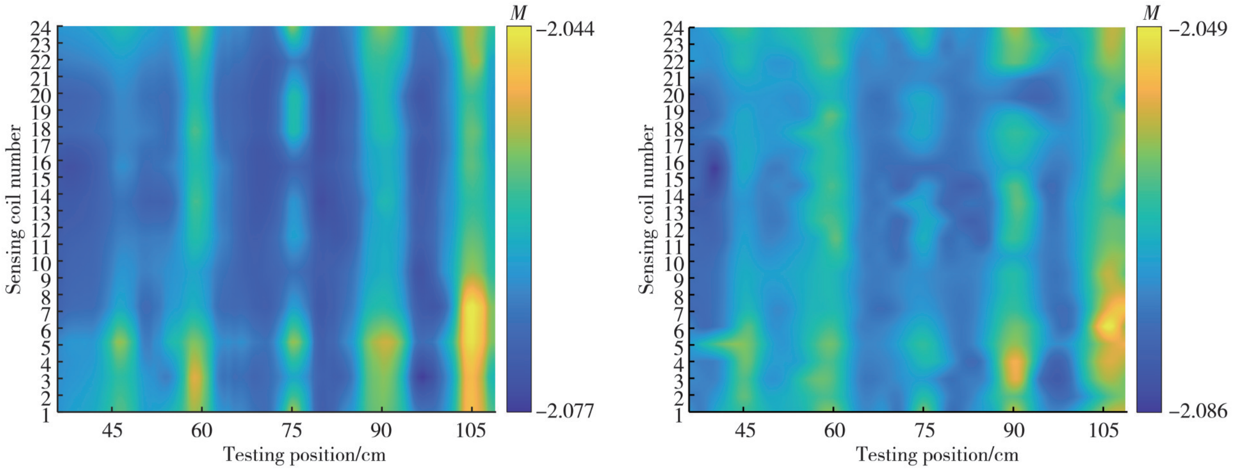

(a) WSTD (b) BEMD

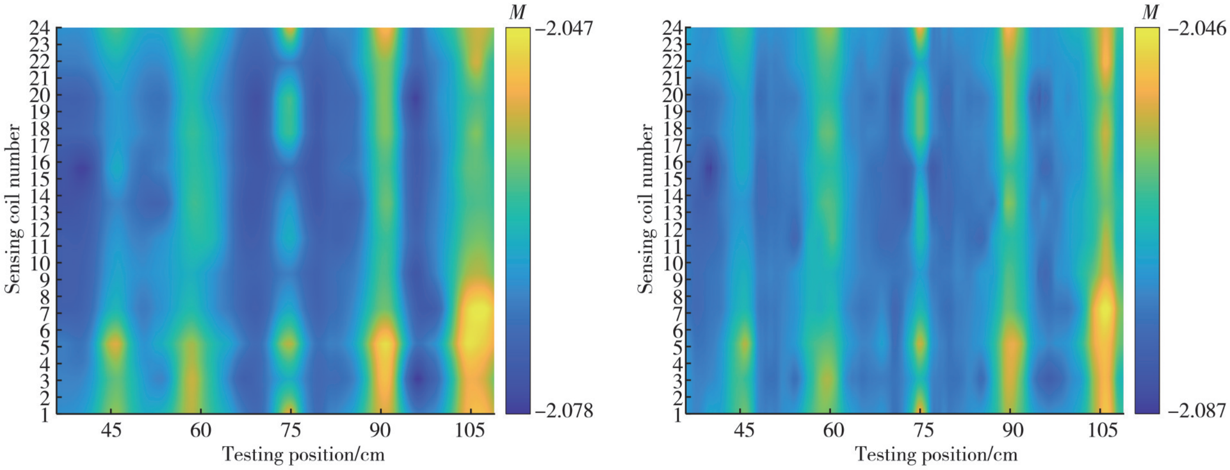

(c) IWTD

(d) BEMD-IWTD

Fig. 14 Comparison of local defect detection images using different denoising algorithms

From a subjective evaluation perspective, the denoising results of ring-shaped and local defect images reveal that although WSTD can suppress background noise to a certain extent, it introduces significant over-smoothing during image reconstruction. This over-smoothing effect leads to the weakening or even loss of some valid defect information, resulting in blurred spacing between ring-shaped defects and poor preservation of fine details in local defect images.

In contrast, IWTD demonstrates better capability in retaining defect structural features while suppressing noise, which helps alleviate the blurring of image details. However, it still suffers from distortion in the defect shapes, making accurate restoration of information challenging. The BEMD method performs denoising by discarding high-frequency IMF components, but since useful defect information is also contained in those high-frequency components, directly removing them leads to the loss of essential details and makes the overall image blurry, obscuring some key defect features. Compared with the above methods, the BEMD-IWTD algorithm refines the high-frequency IMF components with IWTD after BEMD, thus avoiding the loss of effective information caused by simply discarding high-frequency components.

Compared with IWTD alone, this combined strategy allows more precise localization and suppression of noise while preserving image details as much as possible. However, due to the inherently weak defect signals, some information loss remains inevitable, resulting in residual blurriness that still affects accurate defect localization and visualization. To address this issue, we further proposed the BIC image processing algorithm. Based on the effective noise reduction achieved by BEMD-IWTD, CLAHE was introduced for image enhancement, which improved the contrast between defect regions and the background, thereby enhancing defect recognition accuracy and detection performance.

To quantitatively evaluate the improvement in defect detection images, we adopted the defect contrast metric C_d as the evaluation index. Fig. 15 presents the C_d comparison results of different algorithms applied to local defect detection images.

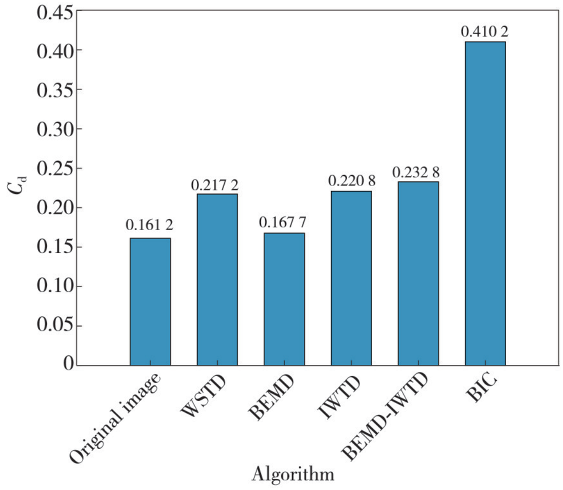

Fig. 15 Comparison of contrast between different algorithms for local defect detection image

It can be seen that BEMD-IWTD improves the defect contrast compared to using BEMD or IWTD alone, indicating that the method effectively suppresses background noise while better preserving defect features, thereby enhancing the visibility of defects in the images. Moreover, the proposed BIC algorithm achieves the highest C_d among all methods, demonstrates superior noise suppression and a notable enhancement in contrast between the defects and the background. This makes the defects easier to identify, thereby improving the accuracy of the detection results.

To verify the superiority of the BIC algorithm, we applied CLAHE, HE, and GT algorithms for enhancement on the defect detection images obtained after BEMD-IWTD processing and conducted a comparative analysis. The ring-shaped defect detection images processed by each algorithm are shown in Fig.16. It can be observed that in the ring defect detection, after applying BEMD-IWTD-HE processing, the image contrast is overly enhanced. This leads to blurred defect boundaries and obscures the morphology, making it difficult to recognize defects clearly. After BEMD-IWTD-GT processing, the intervals of defects with depths of 1 mm and 2 mm become close, affecting the ability to distinguish defects, and decreasing detection accuracy. After BIC processing, background noise is effectively suppressed, and the contrast between the defect and non-defect areas becomes clearer, improving defect recognizability.

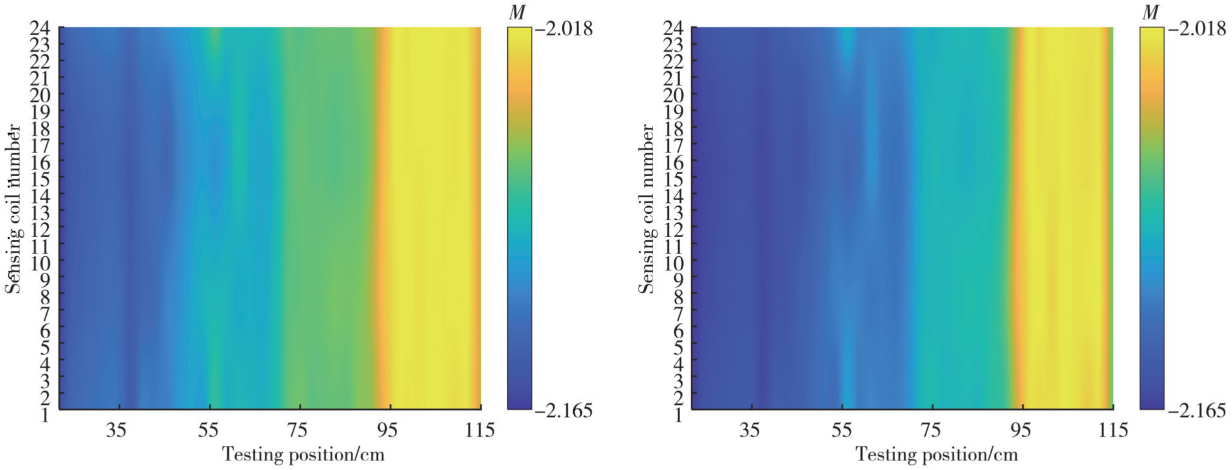

(a) BEMD-IWTD (b) BEMD-IWTD-GT

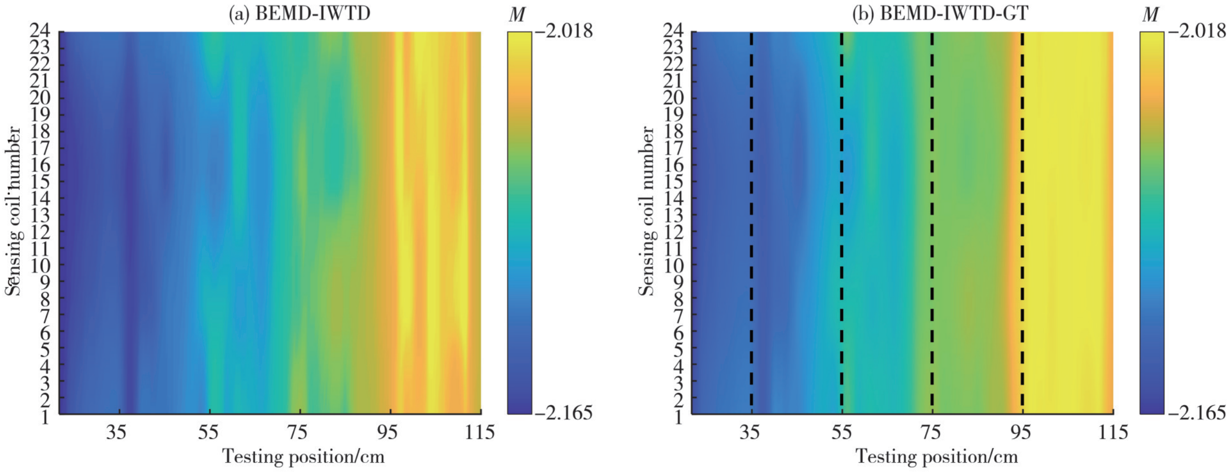

(c) BEMD-IWTD-HE (d) Proposed algorithm

Fig. 16 Comparison of different enhancement algorithms after denoising of ring-shaped defect detection image

The local defect detection images processed by different image processing algorithms are shown in Fig.17. After BEMD-IWTD-HE processing, the defect information is overly enhanced, making it difficult to distinguish the defect positions in the radial direction, affecting the precise localization of defects. After BEMD-IWTD-GT processing, although the defect contrast is enhanced to some extent, the background noise is also amplified, making it difficult to distinguish defects from noise. Processed by the proposed BIC method, the defect contrast is significantly improved, and background noise is effectively suppressed, making the defect morphology clearer and facilitating subsequent automatic defect recognition.

For the local defect detection images, as shown in Table 6, the proposed algorithm provides the highest C_{d} and SSIM, indicating that, while enhancing the defect contrast, it has preserved the structural information of the original image as much as possible, avoiding information loss caused by over-enhancement or over-smoothing. In summary, the BIC image processing algorithm proposed in this study demonstrates superior performance in both denoising and enhancing defect detection images. It can significantly improve the visualization of defects, providing a reliable image basis for subsequent defect recognition and quantitative assessment.

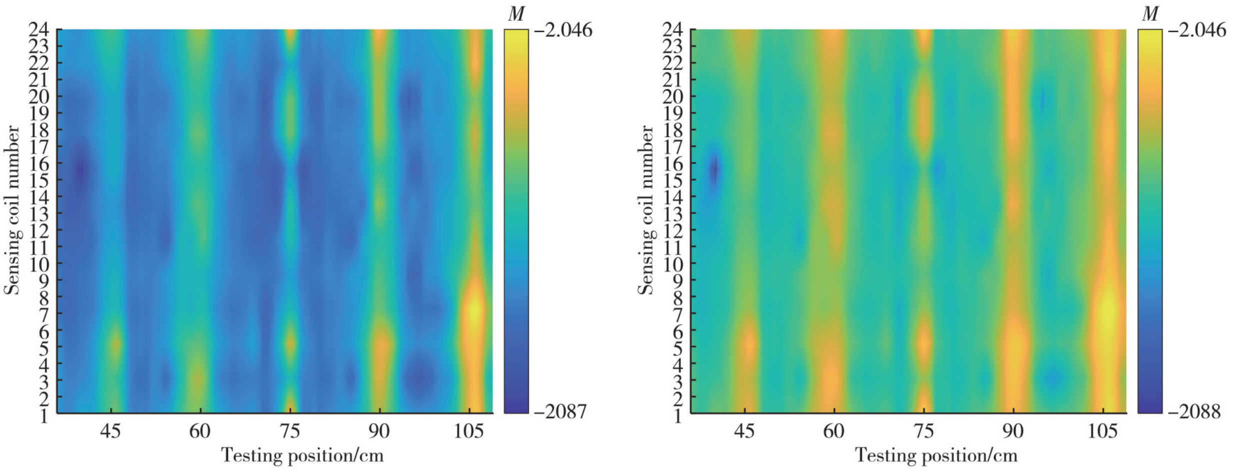

(a) BEMD-IWTD (b) BEMD-IWTD-GT

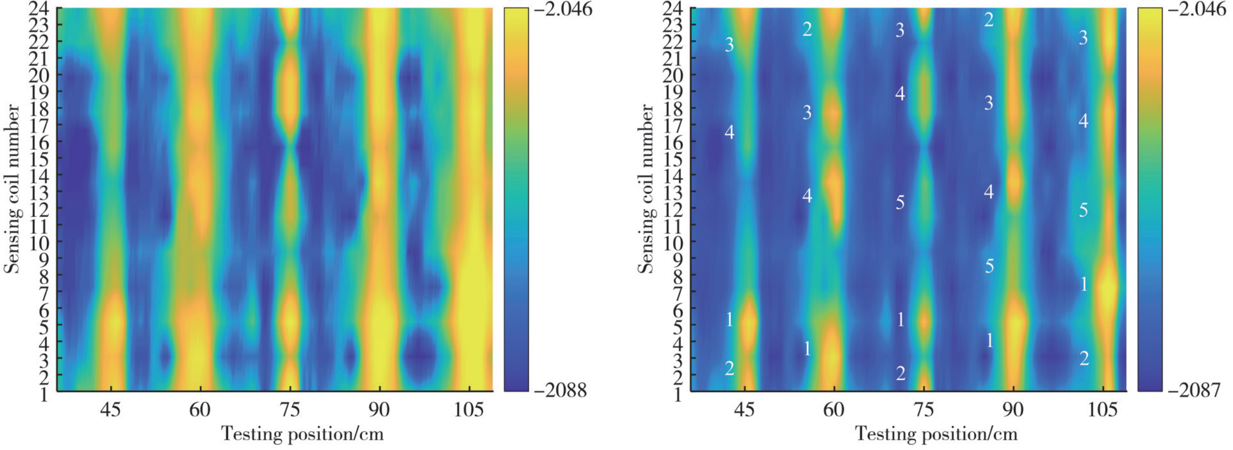

(c) BEMD-IWTD-HE (d) Proposed algorithm

Fig. 17 Comparison of different enhancement algorithms after denoising of local defect detection image

Table 6 Comparison of metrics of different enhancement algorithms after local defect denoising

Algorithm	SSIM	C_d
BEMD-IWTD	1.000 0	0.232 8
BEMD-IWTD-GT	0.716 3	0.174 6
BEMD-IWTD-HE	0.638 8	0.354 1
BIC	0.802 3	0.410 2

4 Conclusions

This study detected defects on the outer wall of ferromagnetic metal casings using near-field pulsed eddy current transient response signal amplitude. Detection experiments were conducted on ferromagnetic metal casings with ring-shaped and local defects, and defect detection images were generated. However, these images were disturbed by noise, affecting the recognition and visualization of the defects. To address this issue, we proposed an image processing algorithm based on BEMD-IWTD combined with CLAHE, called the BIC algorithm. The algorithm first used BEMD-IWTD for denoising to suppress high-frequency noise interference while retaining defect edge information as much as possible. Then, the image contrast was enhanced using CLAHE to highlight the defect features. Experimental results showed that, compared to using BEMD alone, WSTD, IWTD and other image processing methods such as BEMD-IWTD, the proposed BIC method more effectively suppressed noise interference and enhanced the contrast between the defects and the background, significantly improving the defect visualization and recognition capabilities.

Although the proposed BIC algorithm can effectively improve the quality of defect detection images, the BEMD and IWTD processes require a large amount of computational resources. Therefore, the overall processing has relatively high computational complexity and is time-consuming when handling defect detection images, which may limit its practical application in online defect detection systems with high real-time requirements. In future work, the structure of the existing algorithm process will be optimized to reduce redundant computational steps. While ensuring image quality, the overall computation speed will be improved, thereby enhancing the algorithm's real-time adaptability in engineering practice.

Acknowledgement

This work was supported by National Natural Science Foundation of China (No.62303385).

Declaration of conflicting interests

The authors have no conflict of interests related to this publication.

References

[1] LACKEY G, PFANDER I, GARDINER J, et al. Composition and origin of surface casing fluids in a major US oil- and gas-producing region. Environmental Science & Technology, 2022, 56(23): 17227-17235.

[2] DENG K H, LIU W Y, LIU B, et al. Repairing force for deformed casing shaping with spinning casing swage and damage behaviour of cement sheath. Applied Mathematical Modelling, 2019, 70: 425-438.

[3] LACKEY G, RAJARAM H. Modeling gas migration, sustained casing pressure, and surface casing vent flow in onshore oil and gas wells. Water Resources Research, 2019, 55(1): 298-323.

[4] LIU K, GAO D L, WANG Y B, et al. Effect of local loads on shale gas well integrity during hydraulic fracturing process. Journal of Natural Gas Science and Engineering, 2017, 37: 291-302.

[5] SAFAEI A, ASEFI M, AHMADI M, et al. Chemical treatment for sand production control: a review of materials, methods, and field operations. Petroleum Science, 2023, 20(3): 1640-1658.

[6] MUBARAK G, VERMA C, BARSOUM I, et al. Internal corrosion in oil and gas wells during casings and tubing: challenges and opportunities of corrosion inhibitors. Journal of the Taiwan Institute of Chemical Engineers, 2023, 150: 105027.

[7] ZHANG W, SUN H, TAO A H, et al. Local defect detection of ferromagnetic metal casing based on pulsed eddy current testing. IEEE Transactions on Instrumentation and Measurement, 2022, 71: 6003109.

[8] ZHAO X, WANG Z B, LIU B. Phase aberration correction in ultrasonic phased array non-destructive testing systems. Journal of Measurement Science and Instrumentation, 2015, 6(1): 47-52.

[9] GUNARATHNE G P P, QURESHI Y. Development of a synthetic A-scan technique for ultrasonic testing of pipelines. IEEE Transactions on Instrumentation and Measurement, 2005, 54(1): 192-199.

[10] LI B L, SUN C H, XIN S C, et al. Development of a 16-channel broadband piezoelectric micro ultrasonic transducer array probe for pipeline butt-welded defect detection. Sensors, 2022, 22(19): 7133.

[11] TRUSHKEVYCH O, EDWARDS R S. Characterisation of small defects using miniaturised EMAT system. NDT & E International, 2019, 107: 102140.

[12] J. SHULL P. Nondestructive evaluation: theory, techniques, and applications. New York: Marcel Dekker, 2016.

[13] MIN K, RYONG Y, SOO P. Analysis of a defect signal deformations induced by eddy current in RFECT system for pipeline inspection. IEEE Transactions on Magnetics, 2018, 54(11): 6202905.

[14] VASIC D, BILAS V, AMBRUS D. Pulsed eddy-current nondestructive testing of ferromagnetic tubes. IEEE Transactions on Instrumentation and Measurement, 2004, 53(4): 1289-1294.

[15] XU Z Y, WU X J, LI J, et al. Assessment of wall thinning in insulated ferromagnetic pipes using the time-to-peak of differential pulsed eddy-current testing signals. NDT & E International, 2012, 51: 24-29.

[16] ULAPANE N, ALEMPIJEVIC A, VALLS MIRO J, et al. Non-destructive evaluation of ferromagnetic material thickness using Pulsed Eddy Current sensor detector coil voltage decay rate. NDT & E International, 2018, 100: 108-114.

[17] RAO B P C, RAJ B, JAYAKUMAR T, et al. An intelligent imaging scheme for automated eddy current testing. Nondestructive Testing and Evaluation, 2001, 17(1): 41-57.

[18] LI Y, YAN B, LI D, et al. Pulse-modulation eddy current inspection of subsurface corrosion in conductive structures. NDT & E International, 2016, 79: 142-149.

[19] NAFIAH F, SOPHIAN A, KHAN M R, et al. Image-based feature extraction technique for inclined crack quantification using pulsed eddy current. Chinese Journal of Mechanical Engineering, 2019, 32(1): 26.

[20] YAN B, LI Y, REN S T, et al. Recognition and evaluation of corrosion profile *via* pulse-modulation eddy current inspection in conjunction with improved Canny algorithm. NDT & E International, 2019, 106: 18-28.

[21] LI Y, YAN B, LI W J, et al. Pulse-modulation eddy current probes for imaging of external corrosion in nonmagnetic pipes. NDT & E International, 2017, 88: 51-58.

[22] XIE S J, CHEN Z M, TAKAGI T, et al. Quantitative non-destructive evaluation of wall thinning defect in double-layer pipe of nuclear power plants using pulsed ECT method. NDT & E International, 2015, 75: 87-95.

[23] ZHU P P, CHENG Y H, BAI L B, et al. Local sparseness and image fusion for defect inspection in eddy current pulsed thermography. IEEE Sensors Journal, 2019, 19(4): 1471-1477.

[24] YAN B, LI Y, LIU Z S, et al. Pulse-modulation eddy current imaging for 3D profile reconstruction of subsurface corrosion in metallic structures of aviation. IEEE Sensors Journal, 2021, 21(24): 28087-28096.

[25] LI H C, YU Y T, LI L F, et al. A weighted estimation algorithm for enhancing pulsed eddy current infrared image in ecpt non-destructive testing. Applied Sciences, 2019, 9(20): 4199.

[26] REN S, LI Y, LIU Z S, et al. Gradient-field pulsed eddy current imaging of hidden corrosion in layered conductors via

sparse Bayesian learning alongside baseline estimation and denoising with sparsity. Sensors and Actuators A: Physical, 2022, 346: 113900.

[27] ZHU C C, CHEN H Q, ZHU X C, et al. Pulsed eddy current imaging of partially missing solder in brazing joints of stainless steel core plates. Materials, 2024, 17(22): 5561.

[28] BALAKRISHNAN S, CACCIOLA M, UDPA L, et al. Development of image fusion methodology using discrete wavelet transform for eddy current images. NDT & E International, 2012, 51: 51-57.

[29] PARK M, KIM D, OH H S. Quantile-based empirical mode decomposition: an efficient way to decompose noisy signals. IEEE Transactions on Instrumentation and Measurement, 2015, 64(7): 1802-1813.

[30] SADIQ FAREED M M, CHUN Q, AHMED G, et al. Saliency detection by exploiting multi-features of color contrast and color distribution. Computers & Electrical Engineering, 2018, 70: 551-566.

[31] ANNUM R, RIAZ M M, GHAFOOR A. Saliency detection using contrast enhancement and texture smoothing operations. Signal, Image and Video Processing, 2018, 12(3): 505-511.

[32] KALBOUSSI R, ABDELLAOUI M, DOUIK A. Video saliency detection using motion distinctiveness and uniform contrast measure. Informatica, 2019, 30(1): 53-72.

[33] XIE J, XU C H, WU C W, et al. Visualization of defects in CFRP-reinforced steel structures using improved eddy current pulsed thermography. Automation in Construction, 2023, 145: 104643.

基于脉冲涡流检测的铁磁性金属套管缺陷图像处理方法

邓勇^{1,2*}，宋地霖^{1,2}，孙虎^{1,2}

1. 西南石油大学 机电工程学院，四川 成都 610500;
2. 石油天然气装备技术四川省科技资源共享服务平台，四川 成都 610500

摘　要： 油气开采中，铁磁性金属套管是保障油气通道安全的关键设施。但在高温高压环境下，深埋地层中的套管因冲刷和腐蚀易发生变形、扭曲甚至破损，从而导致重大经济损失和人员伤亡。因此，定期检测和维护在役油气井套管至关重要。脉冲涡流检测技术因高效、非接触及信息丰富，被广泛用于套管缺陷检测。然而，检测过程中存在大量噪声，进而影响缺陷检测图像的质量。为解决该问题，针对前期套管缺陷检测图像处理方法进行了研究，提出了基于二维经验模态分解（Bidimensional empirical mode decomposition，BEMD）的改进小波阈值降噪（Improved wavelet threshold denosing，IWTD）结合限制对比度自适应直方图均衡化（Contrast limited adaptive histogram equalization，CLAHE）的图像处理算法（BIC）。该算法首先利用基于BEMD-IWTD对缺陷检测图像去噪，再通过CLAHE增强图像。为验证方法有效性，在含环状和局部缺陷的套管上开展缺陷检测实验，并进行图像处理。经BIC算法处理后，不同深度的环状缺陷可以有效区分，特别是由于噪声影响的1 mm和2 mm深度的缺陷；局部缺陷图像中，原本因噪声干扰难以识别的小尺寸缺陷得以有效识别，缺陷对比度C_d显著提升。实验结果表明，提出的BIC算法能有效抑制缺陷检测图像噪声，增强缺陷与背景对比度，提升缺陷的识别率和检测效果，为后续检测提供可靠的图像处理支持。

关键词： 铁磁性金属套管；无损检测；脉冲涡流检测；缺陷检测；缺陷图像降噪；缺陷图像增强

引用格式： DENG Yong, SONG Dilin, SUN Hu. Image processing method for defect images of ferromagnetic metal casings based on pulsed eddy current testing. Journal of Measurement Science and Instrumentation, 2026, 17(1): 72-87. DOI: 10.62756/jmsi.1674-8042.2026006